

$H\beta$ and $H\gamma$ Absorption-line Profile Inconsistencies in Laboratory Experiments Performed at White Dwarf Photosphere Conditions

M.-A. Schaeuble^{1,3}, T. Nagayama¹, J. E. Bailey¹, T. A. Gomez¹, M. H. Montgomery², and D. E. Winget²
Sandia National Laboratories, Albuquerque, NM 87185, USA; mschaeu@sandia.gov

Department of Astronomy and McDonald Observatory, The University of Texas at Austin, Austin, TX 78712, USA

Received 2019 June 20; revised 2019 September 10; accepted 2019 September 22; published 2019 November 1

Abstract

The spectroscopic method relies on hydrogen Balmer absorption lines to infer white dwarf (WD) masses. These masses depend on the choice of atmosphere model, hydrogen atomic line shape calculation, and which Balmer series members are included in the spectral fit. In addition to those variables, spectroscopic masses disagree with those derived using other methods. Here we present laboratory experiments aimed at investigating the main component of the spectroscopic method: hydrogen line shape calculations. These experiments use X-rays from Sandia National Laboratories Z-machine to create a uniform \sim 15 cm³ hydrogen plasma and a \sim 4 eV backlighter that enables recording high-quality absorption spectra. The large plasma, volumetric X-ray heating that fosters plasma uniformity, and the ability to collect absorption spectra at WD photosphere conditions are improvements over past laboratory experiments. Analysis of the experimental absorption spectra reveals that electron density (n_e) values derived from the H γ line are \sim 34% \pm 7.3% lower than from H β . Two potential systematic errors that may contribute to this difference were investigated. A detailed evaluation of self-emission and plasma gradients shows that these phenomena are unlikely to produce any measurable $H\beta$ - $H\gamma$ n_e difference. WD masses inferred with the spectroscopic method are proportional to the photosphere density. Hence, the measured H β -H γ $n_{\rm e}$ difference is qualitatively consistent with the trend that WD masses inferred from their H β line are higher than that resulting from the analysis of H β and H γ . This evidence may suggest that current hydrogen line shape calculations are not sufficiently accurate to capture the intricacies of the Balmer series.

Unified Astronomy Thesaurus concepts: White dwarf stars (1799); DA stars (348); Laboratory astrophysics (2004); Plasma physics (2089); Atomic physics (2063)

1. Introduction

Hydrogen line shapes have many applications in astrophysics and are of special importance to the field of white dwarf (WD) astronomy (e.g., Bergeron et al. 1992; Tremblay & Bergeron 2009; Koester 2010; Kepler et al. 2015). These line shapes are sensitive to plasma electron temperature (T_e) and density (n_e) at the atmospheric conditions found in hydrogen WDs. By fitting stellar spectra with hydrogen line shape calculations, astronomers are able to derive WD surface gravity (log g) values, which, with the help of evolutionary calculations, can then be converted into stellar masses. Due to the close relationship between log g and stellar mass, these two terms are often used interchangeably. Stellar masses are needed for nearly all WD applications, ranging from determining the age of the universe (e.g., Winget et al. 1987; Fontaine et al. 2001) to deriving the initial-final stellar mass relation for cluster stars (e.g., Cummings et al. 2015, 2016, 2019).

Many theoretical and experimental advances have been made in the physics of hydrogen line shapes over the past several decades (e.g., Berg et al. 1962; Griem et al. 1962; Bengtson et al. 1969; Hill et al. 1971; Wiese et al. 1972; Vidal et al. 1973; Günter et al. 1991; Tremblay & Bergeron 2009; Gomez et al. 2016; Gomez et al. 2018). The Wiese et al. (1972) emission experiments to this day remain the benchmark against which all theoretical calculations are compared, including the models used to infer WD masses. The Vidal et al. (1973) hydrogen line shape theory, also validated using the

Wiese et al. (1972) data, was used in the first large-scale spectroscopic WD mass determination attempt (Bergeron et al. 1992). Soon after the publication of these results, unexpected trends emerged from spectroscopic mass measurements. Bergeron (1993) discovered that including increasingly higher principal quantum number members of the Balmer series in the spectroscopic fit (e.g., fitting only $H\beta$ then $H\beta$ and $H\gamma$, etc.) results in decreasing stellar masses. Since the stellar mass is intimately related to the atmospheric $n_{\rm e}$ (a rise in one causes a rise in the other and vice versa), these results indicate that fitting different Balmer series members results in different $n_{\rm e}$ values for the same plasma.

In addition to this problem, spectroscopically derived masses also disagree with masses derived from other techniques, such as the gravitational redshift (GR; e.g., Falcon et al. 2010; Pasquini et al. 2019) and the photometric method (e.g., Bergeron et al. 2019; Genest-Beaulieu & Bergeron 2019). GR masses are derived from the shift of a spectral line with respect to its rest wavelength. This shift can be converted into a stellar mass using general relativity and the well-constrained WD mass-radius relationship. GR masses can usually only be derived for large $(n \ge 50)$ comoving ensembles of WDs (Falcon et al. 2010). Most WDs are not members of such comoving ensembles, leaving only the spectroscopic or photometric methods as viable mass determination techniques (e.g., Tremblay et al. 2011; Kepler et al. 2015; Tremblay et al. 2019). Joyce et al. (2018) and Pasquini et al. (2019) identify potential uncertainties associated with the GR method. However, since the GR approach depends on different and less complex input physics than the spectroscopic or

 $[\]overline{^3}$ Portions of this work were conducted while a student in the Astronomy Department at the University of Texas at Austin.

photometric techniques, Falcon et al. (2010) have argued that GR masses are more reliable.

The advent of *Gaia* (Gaia Collaboration et al. 2016) has enabled the application of the photometric mass determination technique, which relies on measured fluxes and distances, to large WD samples (e.g., Gentile Fusillo et al. 2019). However, WD mean masses reported by Genest-Beaulieu & Bergeron (2019) and Bergeron et al. (2019) did not conclusively prove the robustness of the photometric technique over other mass determination methods. Further, masses derived from GR, spectroscopy, and photometry do not appear to agree with each other, suggesting that the constitutive physics and models of all these methods need to be scrutinized.

Insufficiently tested hydrogen line shape models have been proposed as the main hypothesis to explain both the n_e trends resulting from fitting individual WD Balmer series members and the mass discrepancies between the spectroscopic and other mass determination methods. The combination of these problems may indicate that current hydrogen line shape theories are not sufficiently accurate to properly model line formation processes in WD atmospheres. The current benchmark experiments (Wiese et al. 1972) reach a maximum n_e of $9 \times 10^{16} \,\mathrm{cm}^{-3}$, while a typical WD atmosphere can extend to an $n_{\rm e}$ of $\sim 1 \times 10^{18}$ cm⁻³. Hydrogen line shape calculations at $n_{\rm e} \gtrsim 1 \times 10^{17}$ cm⁻³ are therefore currently unverified. Additionally, the Wiese et al. (1972) experiments and all theory validations were performed in emission, while WD spectra are collected in absorption. It is generally assumed that these two line profiles are equivalent under the condition of complete redistribution (e.g., Hubeny & Mihalas 2014), but no experimental evidence has been collected to support this premise.

In this paper, we investigate the apparent disagreement in n_e between different members of the Balmer series. The basic hardware layout and experimental procedures of the White Dwarf Photosphere Experiment (WDPE) are described in Section 2. An overview of the WDPE data calibration and n_e extraction method is given in Section 3. The n_e trends resulting from that analysis are discussed in Section 4. Section 5 summarizes potential sources of the n_e disagreement in the WDPE. One such potential source is the self-emission correction of the absorption data. Our investigation reveals that this correction has no impact on our conclusions. The other potential source of the $H\beta$ - $H\gamma$ $n_{\rm e}$ disagreement is plasma gradients, which are outlined in Section 5 and quantified in Section 6 using a combination of experimental data and simulations. The most extreme gradient and its effect on the Hβ-Hγ n_e ratio are presented in Section 7. We find that even the worst-case plasma inhomogeneities cause no significant difference between the $n_{\rm e}$ inferred from different members of the Balmer series. Gradients therefore cannot explain the observed difference between H β and H γ . These findings may have important implications for WD spectroscopic mass determination—namely, that applying emission-validated hydrogen line profile theories to WD absorption spectra may result in incorrect mass measurements of these stars. Furthermore, our results raise questions about the accuracy of current hydrogen line shape models. Additional consequences of our findings for both astro- and plasma physics are given in Section 8.

2. Experimental Platform

Detailed descriptions of the WDPE platform are given in Falcon et al. (2013), Falcon (2014), Falcon et al. (2015b), and Montgomery et al. (2015). The current design of the WDPE platform is called "ACE," which stands for Absorption, Continuum, and Emission (Figures 1 and 2). A single experiment with the ACE platform allows capturing absorption and emission spectra of the same plasma simultaneously. These data sets are collected using the absorption and emission lines of sight (LOSs). Along with those two data sets, the WDPE also records the backlight continuum used to measure absorption with the continuum LOS. In a standard shot setup, ACE usually covers $\sim 0.5 \times 10^{17} \,\mathrm{cm}^{-3} < n_{\mathrm{e}} < \sim 3 \times 10^{17} \,\mathrm{cm}^{-3}$ in a single experiment. This $n_{\rm e}$ (and therefore also $T_{\rm e}$) range is achieved during a single experiment since the plasma is continuously heated by the gold wall (see Figure 1) for about 200 ns (Falcon 2014). The data is time-resolved by recording the plasma spectra on streak cameras. Sample experimental hydrogen spectra recorded with the absorption, emission, and continuum LOSs are presented in Figure 3. The H β emission and absorption features in Figure 3 are similar except for the dip in the center of emission line. The double-peak structure observed in the WDPE emission data is inherent to the H β profile (see Section 2 of Gomez 2017). This double-peak structure is not observed in the WDPE absorption data. A possible explanation for this behavior is additional absorption in the line center resulting from a cold boundary layer plasma. Such additional absorption effects would deepen the dip of the double-peak structure in the emission profile and eliminate it from the absorption feature. Since the double-peak structure is not well understood theoretically (e.g., Gomez et al. 2016), it is difficult to disentangle the additional absorption effects from model uncertainties. Comparisons of H β line shape models and WDPE emission/absorption profiles reveal that this disagreement is limited to the central \sim 5% of the spectral feature and has no measurable effect on the remaining $\sim 95\%$ of the line. We therefore conclude that this effect has no significant impact on the derived H β $n_{\rm e}$ value.

The WDPE platform is designed for use on the Z-machine at Sandia National Laboratories (e.g., McDaniel et al. 2002; Bailey et al. 2006; Rose et al. 2010; Jones et al. 2014; Rochau et al. 2014). Before an experiment, the ACE gas cell (Figure 1) is installed in a large (> $60 \,\mathrm{m}^3$) vacuum chamber, $\sim 324 \,\mathrm{mm}$ away from the Z-pinch dynamic hohlraum radiation source. The cell is then usually filled with ~ 10 torr $(n \sim 7 \times 10^{17} \, {\rm cm}^{-3})$ of H₂ gas. The X-rays produced by the Z-pinch dynamic hohlraum (e.g., Sanford et al. 2002; Bailey et al. 2006) propagate through the vacuum and irradiate a \sim 1.5 μ m thick Mylar window at the front of the gas cell. After having traversed the window, the X-rays then travel through the H₂ gas and impinge on the gold wall, as well as the gold backlighter (see Figures 1 and 2). Consequently, these two gas cell components heat up to a \sim 4 eV temperature. This thermal energy is then reradiated and heats the H₂ gas. The resulting hydrogen plasma reaches a $T_{\rm e}$ of \sim 1.5 eV (Falcon 2014; Falcon et al. 2015b).

The WDPE plasma is observed using three different LOSs, all of which run parallel to the gold back wall (see Figures 1 and 2). The optical fiber/lens system used to collect the absorption data is pointed directly at the backlighting surface. As the photons emitted by the backlighter travel toward the absorption fiber, they get absorbed by the cooler hydrogen plasma, thereby creating an absorption spectrum (see red data

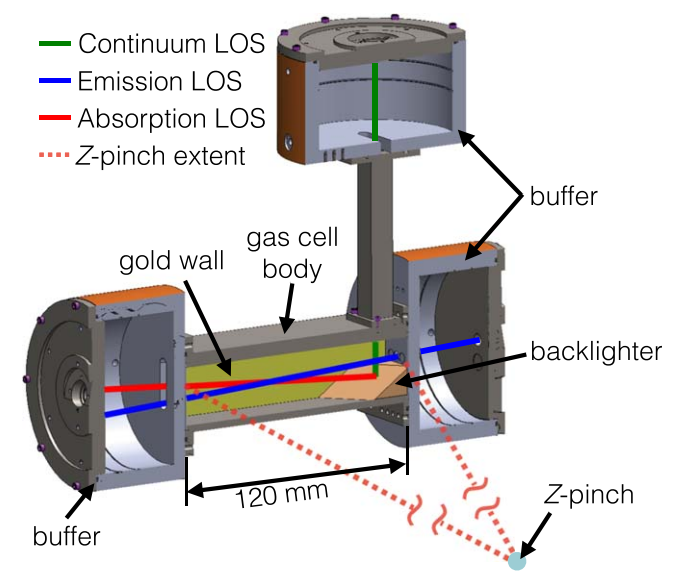


Figure 1. Cross-sectional view of the ACE gas cell. We identify the location of the Z-pinch with respect to the gas cell, as well as all LOSs. Major components of the gas cell are also identified. The H plasma is contained within the gas cell body during an experiment.

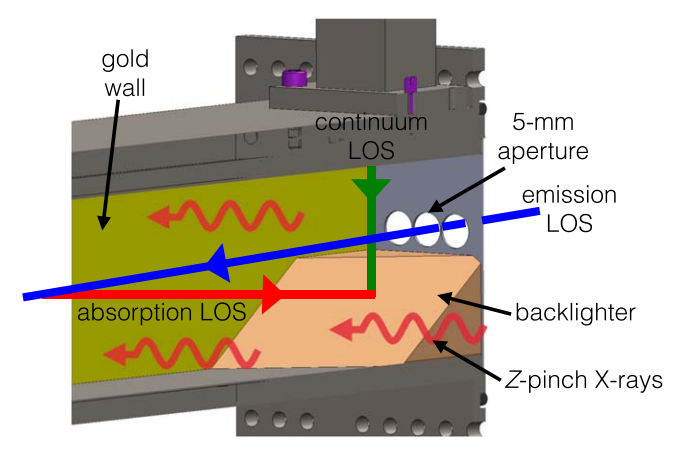


Figure 2. Detailed view of the backlighter. Major gas cell components are identified. We again show the different LOSs identified in Figure 1. The directions of the LOSs are also indicated. The shown *Z*-pinch *X*-rays are perpendicular to the gold wall and backlighter.

in Figure 3). The absorption data probe the lower-level population of any transition under investigation. The continuum LOS fiber/lens system is perpendicularly pointing at the exact same position on the backlighter as the absorption LOS (see Figures 1 and 2). Due to the fact that the continuum LOS traverses ~1.5 mm of heated plasma, rather than 120 mm, small absorption features are expected in this data set (see green spectrum in Figure 3). The emission optical fiber/lens system is not pointing at any hot surface, so only photons emitted by the hydrogen plasma will be captured in this optical path (see blue spectrum in Figure 3). As a counterpart to the absorption data, the emission data can be used to constrain the upper level of any transition under consideration. The data collected from each of these optical paths are recorded on time-resolved spectrometers (Schaeuble 2018).

The advantages of using an experiment as compared to astronomical observations to study uncertainties in hydrogen

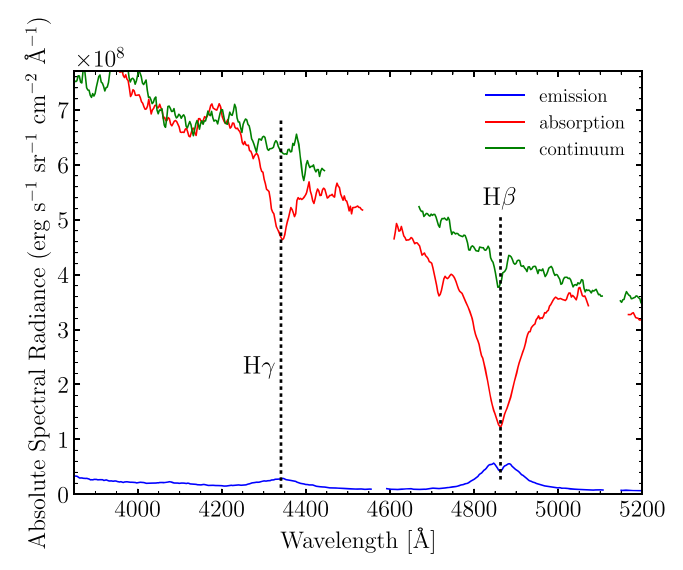


Figure 3. Sample absolute absorption (red), emission (blue), and continuum (green) spectra collected using the LOS setup detailed in Figure 1. We also identify the locations of $H\beta$ and $H\gamma$. These data sets serve as the foundation for our analysis presented in a later section. Spectral regions corrupted by wavelength and timing fiducials have been omitted in this figure.

line profiles are numerous. First, the laboratory plasma composition is known, while that of an astronomical observation is much less certain. Second, an experimental platform can be designed such that plasma inhomogeneities can be characterized and minimized. Third, experiments allow for much greater control over parameters such as plasma $T_{\rm e}$ and $n_{\rm e}$ as compared to astrophysical observations. Finally, experimental reproducibility enables examination of data reliability and accuracy.

3. $n_{\rm e}$ Extraction Method

The ${\sim}34\% \pm 7.3\%$ $n_{\rm e}$ difference between H β and H γ is the main finding described in this paper. WDPE $n_{\rm e}$ values are extracted by fitting hydrogen line shape calculations to the experimental H β and H γ transmission profiles. In this section, we give an overview of the WDPE transmission profile extraction methodology. We restrict this analysis (as all other presented data in this paper) to $t \leqslant 60$ ns after the onset of X-rays (defined to be t=0 ns). The transmission extraction procedure is most reliable at those times. Furthermore, data analysis effects described in Schaeuble (2018) do not affect spectra collected at $t \leqslant 60$ ns.

Three data sets are collected during each WDPE experiment: absorption, emission, and continuum (see Section 2). To extract transmission line profiles from the WDPE data, the collected absorption spectra must be corrected for plasma self-emission. This is achieved by averaging the absorption and emission over 10 ns intervals and subtracting these emission spectra from the absorption data. This calibration step is required since the WDPE backlighter (see Figure 2) is not bright enough to completely overcome self-emission effects in the collected absorption spectra. After the absorption data have been emission corrected, we define a linear continuum across the ${\rm H}\beta$ and ${\rm H}\gamma$ features. The line transmission spectrum, which is a result of the bound–bound absorption process, is then extracted by dividing the emission-corrected absorption data by the defined linear continua. Intensity cross-calibrated absorption

and emission spectra are needed for this transmission extraction procedure.

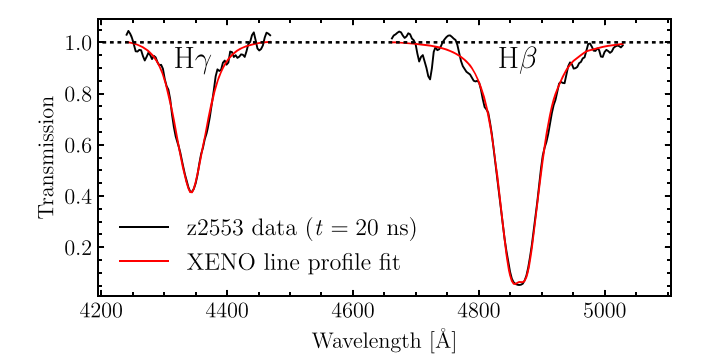
The initial steps of the intensity calibration apply instrument response, fiber transmission, collection solid angle, and spectral intensity corrections to the recorded spectra (Falcon et al. 2015a). After these calibration steps have been completed, all data sets are on an intensity scale. However, since the absorption and emission data are collected on separate cameras, an additional calibration step is needed: quantifying the selfemission correction uncertainty (SECU). The data required to determine the SECU are collected during a so-called calibration shot in which the absorption spectra are collected on their usual camera system, while the continuum data are recorded on the streak camera usually used to capture the emission signal. Such calibration shots are a standard component of a WDPE experimental series. Figures 1 and 2 show that the absorption and continuum LOSs observe the same backlighter region. The intensity-calibrated continuum regions of those data sets therefore should agree. Any offset between the two continuum regions is caused by unaccounted-for effects/errors in the initial intensity calibration steps. We define the SECU as the ratio of intensities recorded on the absorption and continuum LOS systems. Since the calibration shot continuum data is observed on the emission camera system, the derived SECU can be applied to the emission data obtained throughout the same experiment series as the calibration shot. The SECU and its potential to influence the conclusions are described in Section 5.

4. H β and H γ n_e Inconsistencies

Representative fits to experimental data are shown in the top panel of Figure 4. The plotted H β and H γ features depict $n_{\rm e}$ values typical for the WDPE ($n_{\rm e} \sim 1 \times 10^{17} \, {\rm cm}^{-3}$) and also reflect the data quality/fit accuracy we obtain from the WDPE. $n_{\rm e}$ trends as a function of experiment time resulting from H β and H γ transmission fits are shown in the bottom panel of that figure.

Figure 5 shows the H β -H γ $n_{\rm e}$ percent difference as a function of H β n_e for three experiments: z2553 (red), z2787 (green), and z2788 (blue). All of these shots were performed using the same experimental setups. We use four different hydrogen line shape theories to extract the plotted n_e values: Vidal et al. (1973), Gigosos et al. (2003), Tremblay & Bergeron (2009), and Gomez et al. (2016). The n_e inferred by all these theories agree within a few percent (see Falcon et al. 2015b). We therefore only show the theory-averaged percent difference $((n_{eH\beta}-n_{eH\gamma})/n_{eH\beta})$ between H β and H γ n_e as a function of the theory-averaged H β n_e (filled circles in Figure 5). The errors bars in Figure 5 include contributions from uncertainties in the transmission fits, the SECU, and the four different theories used to extract the H β and H γ $n_{\rm e}$ values. Furthermore, we also include $H\gamma$ n_e error contributions stemming from the continuum placement uncertainties of that line. We also show the mean $H\beta$ - $H\gamma$ n_e percent difference for all three shots plotted in that figure as a black solid line. The uncertainty of that mean is shown in gray. The reason for the variance in $H\beta$ – $H\gamma$ n_e disagreement is currently unknown. The average $H\beta$ – $H\gamma$ n_e percent difference is consistent between all three shots (see Figure 5 legend), and it is largely density independent.

From the data shown in Figure 5, we calculate that the n_e values derived from H β in absorption are $\sim 34\% \pm 7.3\%$



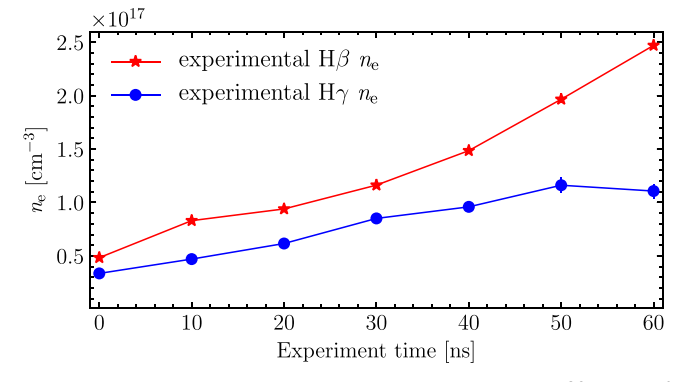


Figure 4. Top: sample line profile fits to the WDPE data using the Xenomorph (Gomez et al. 2016) hydrogen line calculations. Shown here are fits to 10 ns averages of the 20 ns time step in experiment z2553. The derived $n_{\rm e}$ for ${\rm H}\beta$ in this plot is $\sim 1 \times 10^{17} \, {\rm cm}^{-3}$, while the fit to H γ results in $n_{\rm e} = 0.6 \times 10^{16} \, {\rm cm}^{-3}$. Obvious deficiencies in either line profile or fit are not apparent from this plot. Fits for all other shots presented in this paper look similar to the ones shown here. Bottom: H β and H γ $n_{\rm e}$ trends as a function of experiment time for z2553. H β $n_{\rm e}$ values are consistently higher than those inferred from H γ .

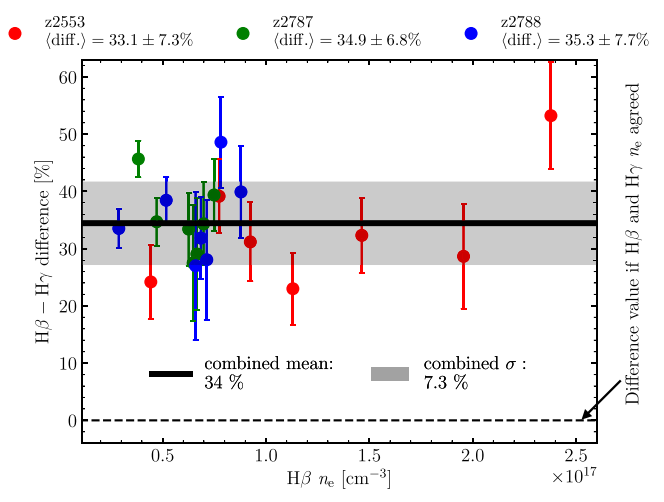


Figure 5. Percent differences between H β and H γ $n_{\rm e}$ as a function of H β $n_{\rm e}$ for shots z2553 (red), z2787 (green), and z2788 (blue). We also show the averaged $n_{\rm e}$ percent difference as a solid back line. The standard deviation in this average is plotted in gray.

higher than those of H γ absorption. The direction of the H β -H γ $n_{\rm e}$ inconsistency agrees with the findings of Bergeron (1993) and Fuchs (2017). A potential explanation for the observed $n_{\rm e}$ discrepancy is inaccurate hydrogen line shape calculations. Flaws in the WDPE data extraction method and inhomogeneities in the experimental platform are other possible reasons for the H β -H γ disagreement. In Section 5, we

investigate these hypotheses and their potential effects on $H\beta\!-\!H\gamma~n_e$ values. The data presented in this paper could potentially be used to study the occupation probability formalism and its influence on the observed absorption lines. However, the importance of this effect increases with n_e . Thus, higher-density WDPE data $(n_e\gtrsim3\times10^{17}~cm^{-3})$ are better suited for such an investigation. These higher-density data are currently being analyzed.

5. Potential Sources of the WDPE H β -H γ n_e Disagreement

5.1. The Dependence of the Derived n_e Values on the Selfemission Correction Uncertainty

The accuracy of the experimental transmission spectra used to derive the $n_{\rm e}$ values plotted in Figure 5 is influenced by the self-emission correction applied to the absorption data. The self-emission correction mainly affects spectral lines with low transmission values (such as $H\beta$) at later experimental times, when the self-emission intensity becomes comparable to that of the absorption feature. We will explore the self-emission correction— $n_{\rm e}$ relationship using shot z2553 (Falcon et al. 2015b). This experiment is the highest- $n_{\rm e}$ data presented in this paper. Any conclusions drawn from its analysis also apply to lower-density data.

The self-emission correction— n_e relationship can be investigated by varying the SECU (see Section 3) applied to the emission data and determining its influence on the final derived n_e values. Shot z2553 has a nominal SECU of 1.4. An upper limit on this nominal self-emission correction uncertainty can be extracted from the requirement that maximum intensity of an emission line *cannot* exceed the minimum intensity of the corresponding absorption line produced in equivalent plasma conditions. The physical reason for this requirement is simple. The absorption-line intensity through a single-temperature plasma slab can be described as follows:

$$I_{\nu,\text{abs}} = B_{\nu} T_{\nu} + \epsilon_{\nu}, \tag{1}$$

while that of an emission line is given by

$$I_{\nu,\text{em}} = \epsilon_{\nu}.$$
 (2)

In Equations (1) and (2), B_{ν} is the intensity at the backside of the plasma (i.e., the backlighter), T_{ν} represents the frequency-dependent transmission of the plasma slab, and the emission intensity is given by ϵ_{ν} . The pure absorption of a plasma can be extracted by measuring the absorption and emission of the same plasma simultaneously and subtracting the two data sets:

$$I_{\nu,\text{abs pure}} = I_{\nu,\text{abs}} - \Phi I_{\nu,\text{em}}.$$
 (3)

 Φ is the SECU in Equation (3). If the measured emission spectrum has a higher intensity than the measured absorption data, a *negative* intensity and transmission will be recovered. This is unphysical and demonstrates that the maximum emission line intensity *cannot* exceed minimum measured absorption-line intensity if both are measured in the same plasma simultaneously.

In the WDPE, we collect absorption and emission data of the same plasma at the same time. We can therefore derive an upper limit on the SECU by setting the maximum $H\beta$ emission intensity equal to the minimum $H\beta$ absorption intensity at t=120 ns after the onset of X-rays. This is the latest time step presented in Falcon et al. (2015b) for shot z2553. We chose the $H\beta$ feature since it is the most optically thick line in our data

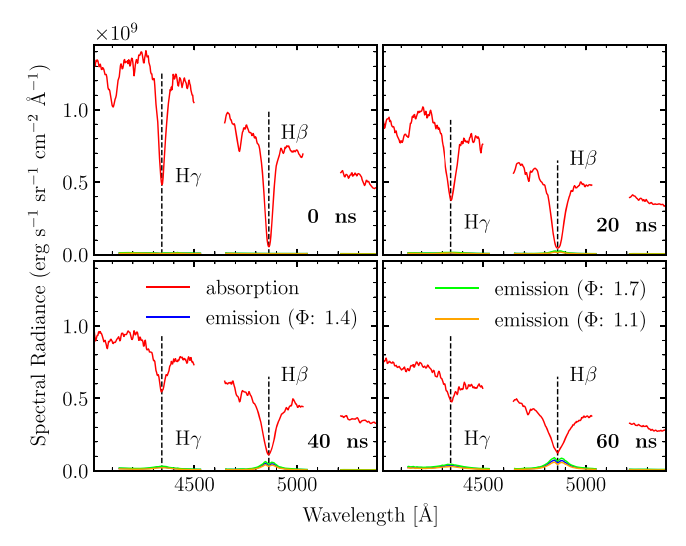


Figure 6. Intensities of calibrated absorption (red) and emission (blue) spectra of shot z2553 at t=0, 20, 40, and 60 ns. The emission spectra have the SECU (1.4) for the z2553 shot series applied to them. We also show emission spectra that have an SECU of 1.1 (\sim 20% lower than nominal SECU; orange) and 1.7 (\sim 20% higher than nominal SECU; green). The orange and green emission profiles are used in the $n_{\rm e}$ sensitivity analysis presented in this section.

(see Figure 3). This procedure results in a maximum SECU of 1.7, a \sim 20% increase over the nominal value. This upper limit applied to all earlier times, since the SECU represents the uncertainty of the self-emission correction, which is most likely independent of time. There exists no equivalent constraint for a lower SECU limit. We therefore adopt 1.1, or a \sim 20% decrease from the initial value, as the lower limit. Furthermore, the exact lower limit is inconsequential since SECU values lower than nominal render self-emission less important.

In Figure 6, we show the time evolution of absorption (red) and emission (blue— Φ : 1.4; orange— Φ : 1.1; green— Φ : 1.7) spectra for shot z2553. It is apparent that for the time range considered in this paper (0 ns $\leq t \leq$ 60 ns after onset of X-rays), emission, regardless of the adopted SECU (compare Equation (1)), never becomes significant with respect to the unattenuated backlight. Therefore, any potential uncertainties in the WDPE calibration and transmission extraction procedures should have minimal impact on the derived experimental $H\beta$ and $H\gamma n_e$. We call attention to the top panels (0 and 20 ns) of Figure 6, where the emission is barely visible. These data demonstrate how small the measured self-emission is with respect to the absorption, regardless of the adopted SECU. The assertion that emission is not significant with respect to the backlight is further confirmed in Figure 7, where we show the H β emission/backlight intensity ratio as a function of experiment time. This ratio is determined by calculating the mean intensity of the emission line between 4800 and 4930 Å and dividing it by the corresponding defined linear continuum of the absorption line. Even in the largest possible emission intensity (i.e., $\Phi = 1.7$) case, the mean emission intensity is only \sim 16% of the absorption value. The maximum change in the H β -H γ $n_{\rm e}$ ratios resulting from SECU variations is \sim 3%. These uncertainties are smaller than other experimental errors. In addition to SECU effects, we also investigated the influence of the continuum placement on the derived n_e values. H γ is weaker than $H\beta$, and it is therefore expected that continuum placement uncertainties have more severe consequences for H γ $n_{\rm e}$. We find that the continuum placement uncertainties have a

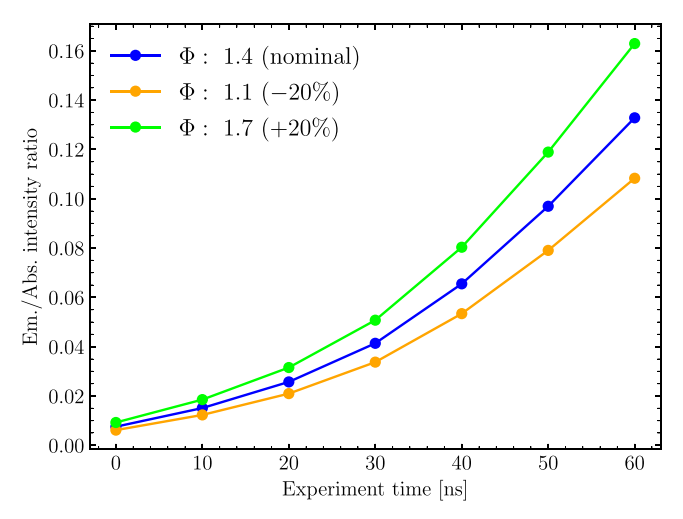


Figure 7. H β emission-to-absorption intensity ratio plotted as a function of experiment time for the SECU values shown in Figure 6. Even in the SECU = 1.7 case (orange), the emission intensity is only ~16% of the corresponding absorption value. These data indicate that within the first 60 ns of the WDPE, emission correction in the extracted transmission spectra is insignificant.

 $\lesssim \! 10\%$ effect on derived H γ $n_{\rm e}$ values, while leaving the H β -H γ $n_{\rm e}$ ratio nearly unchanged. We therefore conclude that within the experimental time range considered in this paper, data calibration, transmission extraction, and continuum placement uncertainties most likely do not present a significant source of error in final derived H β -H γ $n_{\rm e}$ ratio.

5.2. Potential Sources of Gradients in the WDPE Platform

The WDPE platform is designed to provide a uniform plasma. However, no experiment is perfectly homogeneous. In this section, we discuss three sources of inhomogeneities that are directly tied to the hardware of the WDPE: the buffers, the gold wall, and the backlighting surface (see Figures 1 and 2). The potential gradient that might influence the absorption LOS data is somewhat different from that affecting the emission LOS data. However, we demonstrate in Section 5.1 that WDPE emission correction does not significantly change the $n_{\rm e}$ inferred from the H β and H γ transmission profiles. We therefore only discuss potential absorption LOS gradients in this and all succeeding sections.

5.2.1. The Absorption Buffer

The absorption LOS is equipped with a so-called buffer (see Figure 1) to protect the collection optics from the harsh plasma conditions found in the main gas cell body. This buffer is filled with hydrogen gas during an experiment. There is thus the possibility of plasma forming in these hardware regions. As described in Section 4, we focus on the hydrogen Balmer series in the WDPE. The defining feature of that series is the shared n=2 ground state of all member transitions. If the plasma in this buffer reaches sufficient temperatures ($T_{\rm e} \sim 0.8~{\rm eV}$) to promote a significant amount of electrons into the n=2 state (10.199 eV above ground level), these regions could produce absorption features at plasma conditions that differ from those of the main body, thereby influencing our measurements and potentially complicating the data interpretation.

The WDPE design eliminates the direct interaction between the buffer gas and the Z-pinch X-rays. However, the photons

produced by the hydrogen plasma formed in the main gas cell body during an experiment have the potential to heat the buffer gas. This interaction is limited by inserting a 5 mm aperture between the main body of the gas cell and each buffer (see Figure 2). Only one of the 5 mm apertures shown in Figure 2 allows photons to enter the buffer; the other two will be covered by the face of the buffer (which has been omitted from that figure for clarity). We estimate the worst-case buffer-gas cell body plasma interaction by calculating the heating provided by a 1.9 eV blackbody. This temperature represents a ~50% increase over experimentally determined maximum temperature presented in this paper of $\sim 1.30 \, \text{eV}$ (Falcon 2014; Falcon et al. 2015b). Using the hydrodynamics code Helios (MacFarlane et al. 2006), we irradiate a buffer-sized gas slab with the heating provided by this Planckian. We find that, starting from room temperature, the buffer-gas cell body plasma interaction results in a maximum temperature of \sim 0.25 eV in the buffer. Such a temperature is not sufficient to promote a significant number of hydrogen atoms into the n=2 state. According to these calculations, the buffer plasma should therefore not influence the WDPE absorption measurements.

5.2.2. The Gold Back Wall

The gold back wall provides the second potential source of inhomogeneities in the WDPE platform. Due to its relatively large physical extent (120 mm length), the heating provided by this piece of hardware will vary depending on the precise view factor of each plasma location along the gold wall. This view factor effect most likely results in the plasma at the center of the gas cell having the highest temperature. In combination with the large physical extent of the gold wall, this could potentially result in a plasma in which the regions close to the buffers (see Section 5.2.1) are cooler than those at the center of the main gas cell body. Such effects could introduce notable inhomogeneities in the WDPE plasma. These effects will be further investigated in Section 6.

5.2.3. The Backlighting Surface

The backlighting surface provides the photons necessary to measure an absorption spectrum. However, these photons also provide additional plasma heating in the vicinity of the backlighting surface. The influence of this piece of hardware on final plasma conditions can be investigated by performing local thermodynamic equilibrium (LTE) Helios simulations.

Falcon (2014) measured the temperature of the gold backlighting surface as a function of experiment time. He found that this piece of hardware reaches a peak temperature of \sim 4 eV at the beginning of the experiment and cools off to \sim 1.65 eV over 200 ns. Using this temperature history as an input, we simulate resulting hydrogen plasma temperatures and find that a maximum T_e of ~ 2.00 eV is reached at the surface of the gold backlighter. Simulations that compare the relative heating contribution of the gold wall and the backlighting surface reveal that at $\sim 5.8 \, \text{mm}$ from the surface of the backlighter, its plasma heating contribution is equal to that of the gold wall. The backlighter will provide more heating than the gold wall within 5.8 mm of its surface. The relative heating contributions of the gold wall and the backlighter are assumed to be equal in these simulations. However, the heating contribution is directly proportional to the emission surface

area of the element. The gold wall has an emission surface area of $\sim 3900 \, \mathrm{mm^2}$, while the backlighting surface only has an emission area of $\sim 135 \, \mathrm{mm^2}$. The emission area equivalency assumption in the simulations results in an *overestimate* of the temperature increase caused by the backlighting surface. Since the purpose of this paper is to derive the most extreme potential gradients, we will adopt the overestimated temperature and heating distance for our investigation.

6. Constraining Plasma Gradients in the WDPE Gas Cell

We now use experimental data and the considerations presented in Section 5.2 to constrain the gradient along the absorption LOS in the WPDE platform. The most important parameters in any such investigation are $T_{\rm e}$ and $n_{\rm e}$ values. Since all the experiments considered in this paper were performed with a pure hydrogen gas fill, the experimentally determined $n_{\rm e}$ can be directly converted to an LTE $T_{\rm e}$. Falcon et al. (2015b) demonstrate that the LTE assumption is valid at t > 50 ns in the WDPE. As we show later in this section, the most severe gradients in our platform begin at $t \gtrsim 60$ ns, enabling us to derive an LTE temperature from the experimental $n_{\rm e}$.

Detailed experimental line shape measurements are needed for full testing of line shape calculations. Investigating gradients, however, only requires experimental $n_{\rm e}$ and $T_{\rm e}$ values. Therefore, we developed an alternate $n_{\rm e}/T_{\rm e}$ extraction approach that does *not* rely on absolute calibrations or detailed line profile fits and is also much less sensitive to potential uncertainties in the self-emission correction process. Since fewer data calibration steps are needed, this method also enables us to analyze the data much more efficiently. The specifics of this technique, which uses the full width at-half-area (FWHA) to derive the experimental $n_{\rm e}$, are given in the Appendix. All $n_{\rm e}$ values presented in the remainder of this paper are derived using the FWHA method. We note here for completeness that applying the FWHA method to H β and H γ results in $n_{\rm e}$ differences similar to the ones shown in Figure 5.

Applying the FWHA technique to WDPE absorption LOS and continuum LOS data, we can derive a T_e and n_e gradient in an LOS parallel to the gold wall, should such inhomogeneities exist (see "hypothetical gradient" in Figure 8). n_e inferred from the absorption LOS represents the average along the gold wall. The continuum LOS gives a n_e value at the edge of the gas cell (see Figure 8). From these $n_{\rm e}$ measurements, we calculate the continuum LOS/absorption LOS ne ratio. If the plasma is uniform across the gas cell for the duration of the experiment, this ratio will be approximately constant and close to 1. However, if a gradient such as the one shown at the bottom of Figure 8 exists, the continuum LOS/absorption LOS n_e ratio will be smaller than 1 and possibly also time dependent. In either case, the continuum LOS/absorption LOS ne ratio behavior constrains possible inhomogeneities along the gold wall. Potential influences of backlighter heating on the continuum LOS n_e values were considered and found to be negligible. We use five calibration shots to determine the average continuum LOS/absorption LOS n_e ratio. The optical and experimental setup of calibration shots is always the same, making them ideal candidates for this gradient derivation.

Sample area-normalized absorption and continuum calibration shot $H\beta$ spectra in optical depth units at various times are shown in Figure 9. From that figure, differences in absorption and continuum LOS line widths and shapes are apparent. The differences in line shapes can be attributed to the increased

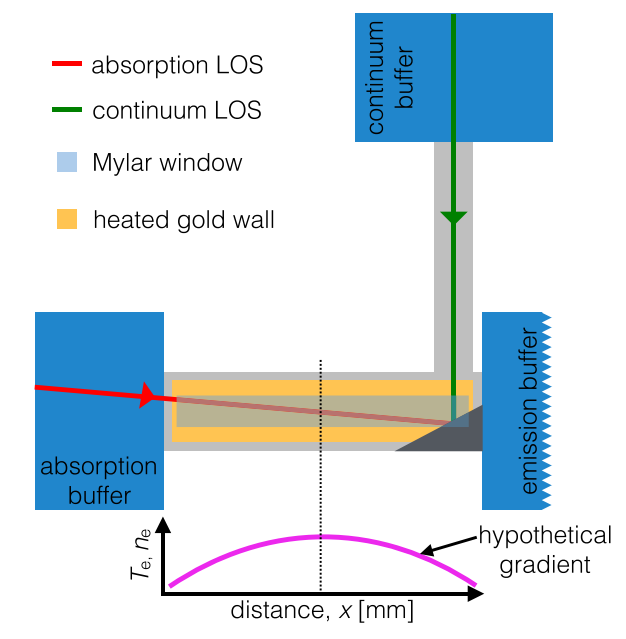


Figure 8. Comparison of absorption (red) and continuum (green) LOS optical paths. The absorption LOS integrates along the gold back wall, while the continuum data set allows us to measure the $n_{\rm e}$ values at the edge of the gas cell.

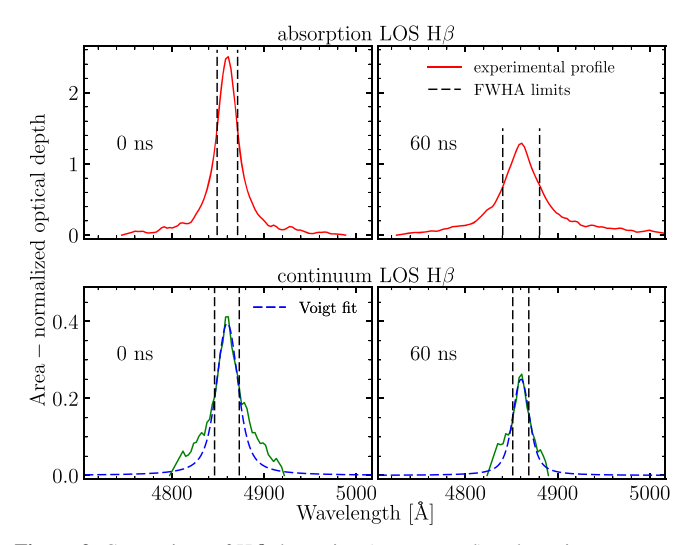


Figure 9. Comparison of $H\beta$ absorption (top row, red) and continuum spectra (bottom row, green). We also show Voigt fits (bottom row, blue dashed) to the continuum LOS data.

influence of the backlighter on the continuum LOS data (see Figure 1). As we discuss in Section 5.2.3, the backlighter produces a $T_{\rm e}/n_{\rm e}$ gradient within ~ 5.8 mm of its surface. Broader line absorption features from this 5.8 mm thick plasma affect the 20 mm long continuum LOS more severely than the 120 mm long absorption LOS. The stronger relative influence of the backlighter on the continuum LOS manifests itself in a broad absorption background to the main H β line. Such a feature is clearly visible in the bottom left panel of Figure 9. To minimize the impact of this background feature on the continuum LOS $n_{\rm e}$, we fit a Voigt profile (blue dashed line in Figure 9) to the central component of the continuum LOS H β feature. The continuum LOS FWHA and $n_{\rm e}$ values are inferred from these Voigt fits. Tests have shown that the $n_{\rm e}$ inferred

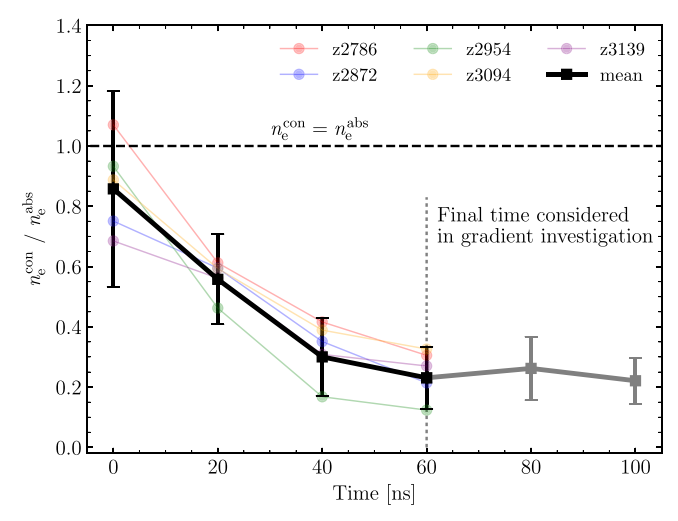


Figure 10. Ratio of $n_{\rm e}$ values inferred by the continuum data to those derived from the absorption data. We also show the mean ratio (black line) and its standard deviation derived from all shots. The $n_{\rm e}$ values shown in this plot are derived from uncorrected absorption and continuum data. For the gradient investigation presented here, we did not consider any data at t > 60 ns (gray dashed line). We show the trend of the continuum/absorption $n_{\rm e}$ ratio beyond those times with a solid gray line.

directly from the profile and those obtained from the Voigt fits differ by \lesssim 5%.

The absorption-continuum LOS line width discrepancies indicate a genuine $n_{\rm e}$ difference between these data and serve as experimental evidence for a time-dependent gradient within the WDPE platform. The absorption spectra are generally first processed in absolute units (see Figure 3; Falcon et al. 2015b) and converted to transmission by defining a linear continuum across the H β spectral features. After dividing by that continuum, the optical depth is extracted taking the natural logarithm of the transmission profile. The left column in Figure 9 depicts data at t = 0 ns, while the right column gives the data at t = 60 ns. The H β features presented in this figure demonstrate that the continuum and absorption LOSs are exposed to a different n_e evolution during a single experiment. At t = 0 ns, the derived FWHA values for the continuum and absorption H β lines are consistent with each other. The data collected at t = 60 ns indicate growth in the absorption FWHA value, while that of the continuum has decreased. These trends imply that the absorption LOS plasma becomes increasingly dense at the center of the gas cell, while the continuum LOS, which only observes the edge plasma, collects data of a plasma with decreasing density. Any continuum data observed at late times (t > 60 ns) suffers from signal-to-noise issues. n_e values derived from the continuum LOS at t > 60 ns should thus be consumed with caution.

We plot the continuum LOS/absorption LOS $n_{\rm e}$ ratios as a function of time for five shots in Figure 10. The continuum LOS/absorption LOS ratios from individual shots are given in color, while their mean is given in black. The standard deviation of the mean is calculated from the scatter in the continuum LOS/absorption LOS $n_{\rm e}$ ratios. Given the limitations of the continuum data outlined above, we do not consider any $n_{\rm e}$ beyond $t=60\,{\rm ns}$ in this paper. However, we plot the mean continuum/absorption $n_{\rm e}$ ratio in Figure 10 beyond $t=60\,{\rm ns}$ in gray to demonstrate that after this time the continuum/absorption $n_{\rm e}$ ratio stabilizes for all shots. This trend indicates that the maximum continuum/absorption $n_{\rm e}$

difference, and therefore also the plasma gradient, is reached at $t \gtrsim 60$ ns. Hence, any gradient derived using the t = 60 ns data should represent an upper gradient limit for all time steps considered in this paper. We currently do not know the source of the variance in the continuum LOS/absorption LOS n_e ratio. Since this spread seems to dominate at early times, we are not concerned with its effect on the derivation of the final gradient.

From Figure 10, it is clear that the $n_{\rm e}$ difference between the center and edge of the gas cell evolves over time. This effect may be attributed to increasingly differential heating in the gas cell. One potential explanation for the differential heating is changing plasma opacities. Early in time, the hydrogen plasma has a relatively low opacity, allowing the gold wall photons to heat the entire plasma almost uniformly. We still expect the edges of the plasma to exhibit a lower $n_{\rm e}$ than the main plasma body in this stage owing to gold wall view factor effects. Later in time, view factor considerations are compounded by the increasing plasma opacity. Photons are now no longer heating the plasma uniformly, but are trapped in the center of the gas cell. The combination of these two effects leads to a steady decrease in the continuum/absorption $n_{\rm e}$, just like we observe in the experimental data.

7. The Impact of Gradients on Absorption n_e Values

7.1. Deriving the WDPE Plasma Gradient

The continuum LOS/absorption LOS n_e ratio presented in Figure 10 helps constrain the plasma gradient along the gas cell (x in Figure 8). As evident from Figure 10, the continuum LOS/absorption LOS n_e ratio stabilizes at ~ 0.25 . From the experimental data at the times where the ratio has stabilized, we can derive $n_{\rm e\ max,\ absorption\ LOS} \approx 2.42 \times 10^{17}\ {\rm cm}^{-3}$, while $n_{\rm e\ max,\ continuum\ LOS} \approx 0.60 \times 10^{17}\ {\rm cm}^{-3}$. The combination of absorption $n_{\rm e}$ values, the measured total particle density, and the Saha equation leads to an LTE $T_{e \text{ max, absorption LOS}}$ of \sim 1.30 eV (Falcon et al. 2015b). The sole electron donor in our plasma is hydrogen, and it only possesses a single electron. In the experimental $T_{\rm e}$ range presented in this paper $(0.8 \,\mathrm{eV} \lesssim T_\mathrm{e} \lesssim 1.3 \,\mathrm{eV})$, increasing temperature directly leads to a higher hydrogen ionization fraction and plasma n_e . The WDPE gradient must therefore exhibit a higher temperature in the main body (which is probed by the absorption LOS) than on the edges of the gas cell (observed by the continuum LOS).

We combine the n_e and T_e constraints supplied by the continuum and absorption LOSs with the physical dimensions of the gold wall to iteratively derive a gradient in the WPDE. This gradient is assumed to reach the highest temperature in the center of the gold wall and linearly decrease to the edges. In the first step of our iterative procedure, we assign guessed $T_{\rm e}$ values to the center and edge of the gold wall. This Te gradient is converted to an n_e trend using Spect3D (MacFarlane et al. 2007) under the assumption of a pure hydrogen plasma in LTE with a uniform particle number density. We then incorporate the effects of the gold backlighter (see Section 5.2.3) into this initial guess gradient. The mean T_e and n_e of this initial gradient estimate are then compared to the experimental absorption LOS data. Since we have defined this first-guess gradient to be a function of distance along the gold wall, we also compare the $n_{\rm e}$ of the initial estimate to the experimental continuum LOS data at the corresponding distance. We iteratively update the center and edge T_e values until agreement between all T_e and n_e constraints is reached. The influence of the gold backlighter is

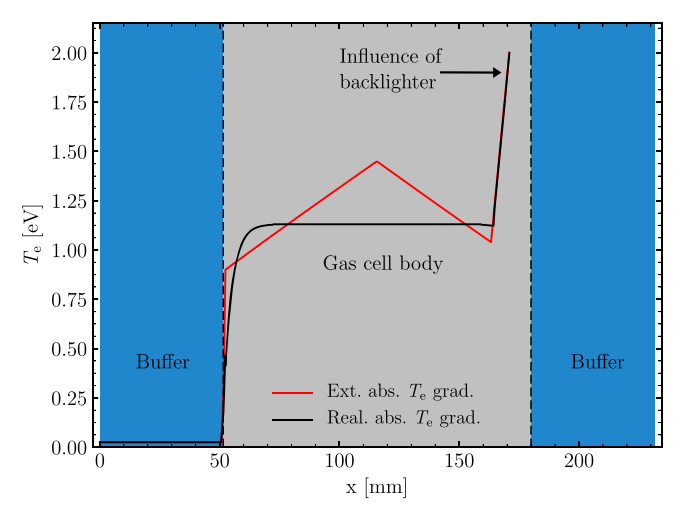


Figure 11. $T_{\rm e}$ gradients in the WDPE as a function of distance from the absorption LOS fiber/lens system. We show the adopted, extreme version of this gradient in red ("Ext."), while the more realistic version ("Real.") is plotted in black. We identify major hardware regions of the gas cell and also highlight the influence of the backlighter.

always taken into account during these $T_{\rm e}$ iterations. Using this procedure, we derive a gradient that has a maximum temperature of 1.45 eV at the center of the gas cell and drops to $0.90 \,\mathrm{eV}$ at the edges. The T_e and n_e gradients derived in this manner are shown in Figures 11 and 12. We label them "Ext." since they represent the most extreme version of inhomogeneities in the WDPE. For comparison purposes, we also show gradients in those figures that were derived by only considering gold wall view factor effects on plasma heating. We believe that these gradients (labeled "Real." in Figures 11 and 12) are much more plausible. For the purposes of the current investigation, we adopt the extreme gradients. This approach ensures that we are not underestimating their effects on the WDPE experimental data. The reader is reminded, however, that the adopted/extreme gradient (see Figures 11 and 12) does not represent a physically realistic situation by any means.

7.2. $H\beta$ and $H\gamma$ n_e Resulting from Plasma Gradient

We calculate synthetic spectra under the influence of the extreme gradients shown in Figures 11 and 12 using Spect3D (MacFarlane et al. 2007). The H β and H γ $n_{\rm e}$ values are then extracted from the simulated data using the FWHA method. For H β , we recover an $n_{\rm e}$ of 2.37×10^{17} cm⁻³, while analysis of H γ results in 2.32×10^{17} cm⁻³. These $n_{\rm e}$ values agree to within $\sim 2\%$. It therefore seems unlikely that plasma gradients are responsible for the observed $\sim 34\%$ difference in $n_{\rm e}$ from H β and H γ . An investigation of the profiles calculated from the realistic gradients shown in Figures 11 and 12 gives similar results. For completeness, we note here that gradients in the vertical direction as well as across each LOS were also investigated in this study. These plasma inhomogeneities were found to be negligible.

8. Conclusions

In this paper, we present laboratory measurements of $H\beta$ and $H\gamma$ absorption n_e discrepancies. Our results show n_e trends similar to those found in the analysis of WD absorption spectra (Bergeron 1993; Fuchs 2017). A direct comparison of the results presented in this paper to Bergeron (1993) and

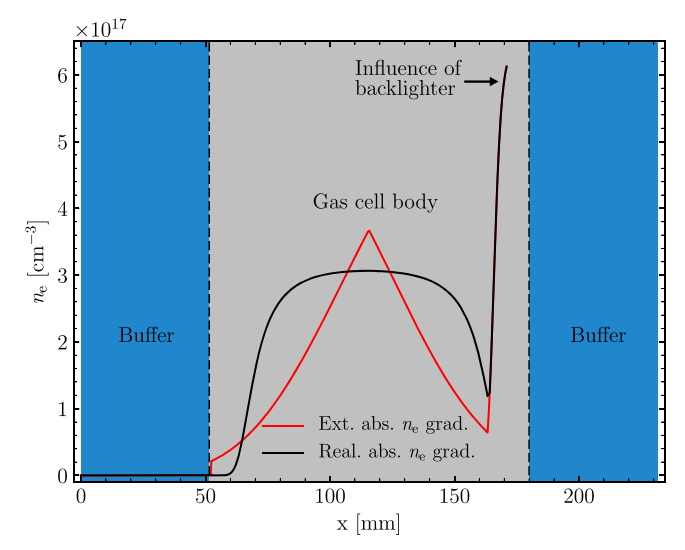


Figure 12. $n_{\rm e}$ gradients resulting from the $T_{\rm e}$ gradients shown in Figure 11. As in Figure 11, the extreme $n_{\rm e}$ trends are shown in red ("Ext."), while the more realistic version is plotted in black ("Real."). We identify major hardware regions of the gas cell and also highlight the influence of the backlighter.

Fuchs (2017) is difficult since synthetic and real WD spectra used in the spectroscopic method are integrated over the entire stellar photosphere. These photospheres can cover several orders of magnitude in n_e and several factors in T_e . The WDPE probes single n_e - T_e combinations. The WD n_e disagreements between different members of the Balmer series are thought to be at least partly responsible for a serious problem in WD astronomy: the discrepancy between WD masses derived from spectroscopy and those resulting from the GR and photometric methods (e.g., Falcon et al. 2010; Bergeron et al. 2019; Genest-Beaulieu & Bergeron 2019; Pasquini et al. 2019). This mass uncertainty prevents the calculation of reliable WD luminosity functions, which are needed to apply these stars to one of astronomy's most pressing problems: the age of the universe (e.g., Winget et al. 1987). WD mass uncertainties also hinder the derivation of accurate mass-loss models (e.g., Cummings et al. 2019). Such models are important for the understanding of Galactic and stellar evolution (e.g., Agertz & Kravtsov 2015). It is currently unknown whether the WDPE data presented in this study fully explain the $n_{\rm e}$ trends observed in the spectroscopic method. However, given that photometric and GR mass measurements generally disagree with those resulting from spectroscopic fits, it is not inconceivable that the steady decrease in ne inferred from increasingly higher principal quantum number members of the Balmer series we derive from the WDPE is related to this astrophysical problem. More research to establish such a link is required.

To ensure that our results are not influenced by experimental uncertainties, we investigate two potential systematic errors in this paper. In Sections 3 and 5.1, we explore the importance of emission subtraction on the final derived $H\beta$ – $H\gamma$ n_e values. Potential plasma inhomogeneities in the WDPE, which could also alter the n_e derived from spectral lines, are explored in Section 5.2. Our investigations suggest that neither the uncertainties in the transmission extraction method nor the plasma inhomogeneities can explain the experimentally observed $\sim 34\% \pm 7.3\%$ $H\beta$ – $H\gamma$ n_e difference.

Tremblay & Bergeron (2009) suggest that the H β -H γ $n_{\rm e}$ difference in WD observations first reported by Bergeron (1993) may be caused by nonideal equation-of-state effects. We

fit the WDPE data with the Tremblay & Bergeron (2009) profiles, which contain corrections for such nonideal effects. We also fit the WDPE data with the Gomez et al. (2016) models, which take an altogether different line shape calculation approach. However, interpretation of the data using both of these profiles still results in a $\sim 34\%$ H β -H γ $n_{\rm e}$ difference. Nonideal effects therefore cannot explain the H β -H γ $n_{\rm e}$ difference presented in this paper. Further investigation into the apparent disagreement between the results presented in this paper and those discussed in Tremblay & Bergeron (2009) is needed.

It is currently unknown which of the two experimental plasma n_e measurements (H β or H γ) more closely mirrors the true plasma n_e value. Helios simulations of the WDPE plasma agree with the experimental H β n_e values. The results of such simulations depend heavily on atomic input data (opacities, level structure, etc.), which we assume to be well known for hydrogen. Furthermore, current hydrogen line shape calculations used in the spectroscopic method and the WDPE are based on perturbative theory (e.g., Vidal et al. 1970). At the plasma conditions presented in this paper, H β is less perturbed than H γ , indicating that models should be more accurate for the former. The combination of theoretical evidence suggests that H β is the more accurate line, but only independent determination of the WDPE plasma n_e will be able to verify this preliminary conclusion.

The data analysis method examination and gradient investigation we describe in this paper are a first step toward understanding the disagreement in the WDPE $H\beta$ – $H\gamma$ absorption $n_{\rm e}$ values. However, the source of the discrepancy remains unknown. One potential explanation could be that our current investigation failed to account for an important and unknown experimental effect. Such issues could be explored by deriving a space-resolved gradient in the gas cell or employing an independent n_e diagnostic to diagnose the plasma. Another reason for the observed n_e difference could be weaknesses in current hydrogen line shape theories. All such calculations are validated in emission using the Wiese et al. (1972) data. To our knowledge, no experiment has ever attempted to validate hydrogen line shapes in absorption. If line profile calculations are found to be deficient, new input physics for those models must be developed. On the other hand, if the hydrogen line profile calculations are sound, could past comparisons to the Wiese et al. (1972) data or those experiments be flawed? This possibility will be difficult to investigate. A fundamental question arising from our investigation is whether the concept of complete redistribution, which leads to equal absorption and emission features, is a valid assumption for astrophysical plasmas. The answer to this final question could have major implications for many areas of astro- and plasma physics.

This work was performed at Sandia National Laboratories. We thank the Z-facility teams and in particular G. Loisel, D. Scogiletti, S. Patel, D. Begay, D. Bliss, K. Shelton, A. York, and K. MacRunnels for their support. Sandia National Laboratories is a multimission laboratory managed and operated by National Technology and Engineering Solutions of Sandia, LLC, a wholly owned subsidiary of Honeywell International, Inc., for the U.S. Department of Energy's National Nuclear Security Administration under contract DE-NA-0003525. This paper describes objective technical results and analysis. Any subjective views or opinions that might be

expressed in the paper do not necessarily represent the views of the U.S. Department of Energy or the United States Government. We thank our reviewers for their comments, which helped make this paper stronger. We also thank Alan Wootton and Greg Rochau for championing our fundamental science research efforts. M.S. thanks R.F. for his help in collecting the WDPE data. M.S., M.H.M, and D.E.W. acknowledge support from the Wootton Center for Astrophysical Plasma Properties under the United States Department of Energy collaborative agreement DE-NA0003843, from the United States Department of Energy grant under DE-SC0010623, and from the National Science Foundation grant under AST 1707419.

Appendix n_e **Determination Methodology**

Deriving the $n_{\rm e}$ at various locations in the WDPE gas cell is crucial for constraining plasma inhomogeneities in the WDPE. The absorption optical path can be used to extract the integrated $n_{\rm e}$ along the gold wall, while the continuum LOS allows for an $n_{\rm e}$ measurement at the very edge of the gas cell (see Figure 1). These two data points serve as an important constraint for the $T_{\rm e}$ and $n_{\rm e}$ trends along the absorption and emission LOSs. In previously published work (e.g., Falcon et al. 2015b; Montgomery et al. 2015), we employed an $n_{\rm e}$ extraction approach that relied on absolutely calibrated emission-corrected absorption spectra and detailed line shape calculations. While this method produces highly accurate results, it also requires many complicated calibration measurements. Furthermore, absorption and emission data sets of the same plasma are required to extract the desired $n_{\rm e}$ values.

During WDPE calibration shots, whose data are used to constrain the plasma gradients presented in Section 6, two absorption spectra are collected. The above-described method of extracting n_e values is thus not applicable. An obvious alternative is the FWHM metric for H β (e.g., Vidal et al. 1973; Gigosos & Cardeñoso 1996; Lemke 1997). However, WDPE experimental spectral features are optically thick in their cores and also suffer from the influence of plasma inhomogeneities in the line centers. The combination of these effects makes the FWHM measurement a suboptimal n_e derivation method for the data presented in this paper. A more appropriate n_e extraction approach for the WDPE data is the FWHA technique discussed in, among other papers, Gigosos et al. (2003). The FWHA method relies on the integration of the entire line profile and subsequent determination of limits that reduce the integral to 50% of its initial value. The FWHA method has several advantages over the FWHM approach. From a theoretical standpoint, the FWHA method is much less susceptible to inaccuracies in the ion-dynamics and electron-broadening approximations of the line shape calculation. Ion-dynamics are especially important for the H β line that is being used as an electron density diagnostic in this paper. From an experimental point of view, the FWHA method is less sensitive to optical depth and plasma gradient effects compared to the FWHM approach.

To demonstrate that the FWHA method produces $n_{\rm e}$ results comparable to detailed line shape fits, we compared the results of the two techniques using shot z2553 (Falcon et al. 2015b). To extract the FWHA $n_{\rm e}$ values from z2553, we first normalized the experimental H β absorption line. This converts the spectral feature to transmission, and in the final step we convert to optical depth units. Figure 13 shows representative

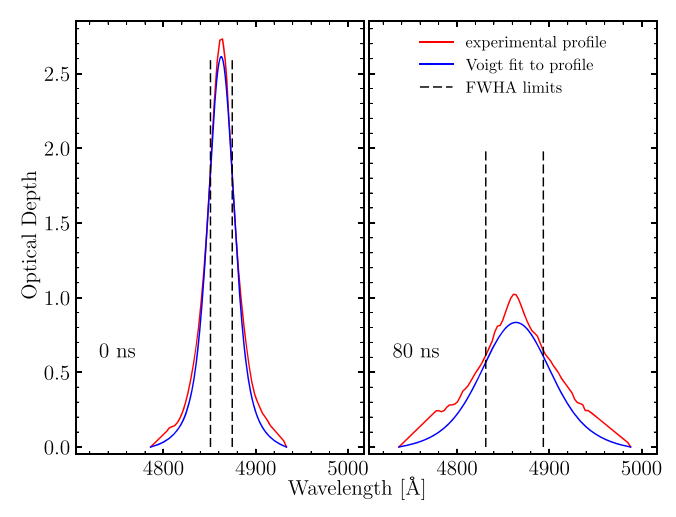


Figure 13. Absorption-line transmission profiles for two different time steps in our experiment. These profiles are from shot z2553. We also show fits of a Voigt profile to the data, as well as FWHA limits for the experimental profile.

experimental $H\beta$ profiles at different times. We also display the FWHA limits of the observed line profile (black dashed lines), as well as Voigt line profile fits.

An analysis of theoretical line profiles is required to translate the FWHA values determined from the experimental features into n_e values. Accounting for instrumental effects in the WDPE data is now required. We use the Xenomorph line profiles (Gomez et al. 2016) to derive the FWHA $-n_e$ relation. As is the standard in the theory community, these line shapes are area normalized. To extract transmission spectra from these calculations, we multiply the area-normalized theoretical line profile by the integral value of the experimental feature and take the exponential of that product. We then convolve the synthetic spectrum with a 12 Å Gaussian that mirrors the instrumental broadening. Since this broadening is much smaller than the nominal line width for the experimental H β profiles (\sim 60 Å), we do not expect this step to influence the derived $n_{\rm e}$ values. The instrumentally broadened theoretical transmission profile is then converted back to optical depth and used to extract the desired FWHA- n_e relationship. This process is repeated for all available theoretical H β line profiles at temperatures ranging from ~ 0.7 to $\sim 1.9 \, \text{eV}$ that were calculated under the assumption of a pure hydrogen plasma. Figure 14 shows the final FWHA- n_e relationship we derive from the approach. The n_e region applicable to the WDPE is highlighted in green. Since the FWHA is almost exclusively a function of plasma $n_{\rm e}$, temperature effects can be ignored (see, e.g., Table 25 of Gigosos & Cardeñoso 1996).

Now that we have fully described our method of extracting an FWHA– n_e relationship from the Gomez et al. (2016) line profile calculations, we will apply it to shot z2553. The results of this analysis are given in Figure 15. We show the n_e values derived from detailed line profile fits to the emission-corrected absorption spectra (see Section 3) in blue. The n_e values extracted by applying the FWHA method to *uncorrected* absorption spectra are depicted in red. The n_e values derived by the two methods agree well. This justifies using the FWHA approach to extract n_e values from our experimental data. Using uncorrected absorption profiles to derive n_e values is also validated by Figure 6, which shows that the emission correction is insignificant within the first \sim 60 ns of the experiment.

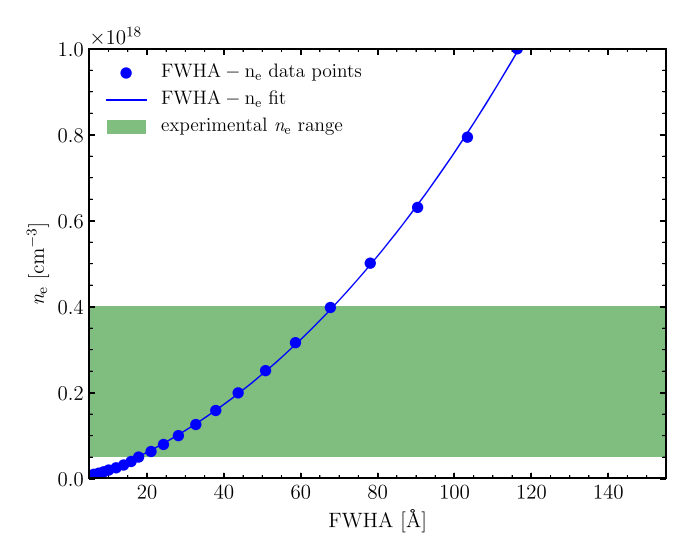


Figure 14. Nominal FWHA– n_e relationship resulting from the analysis of the Xenomorph data. We show the data points extracted from the Gomez et al. (2016) profiles, as well as the second-order polynomial fit to those points. Clearly, the second-order fit nicely reproduces the data points. The n_e region covered by the experiment is highlighted in green.

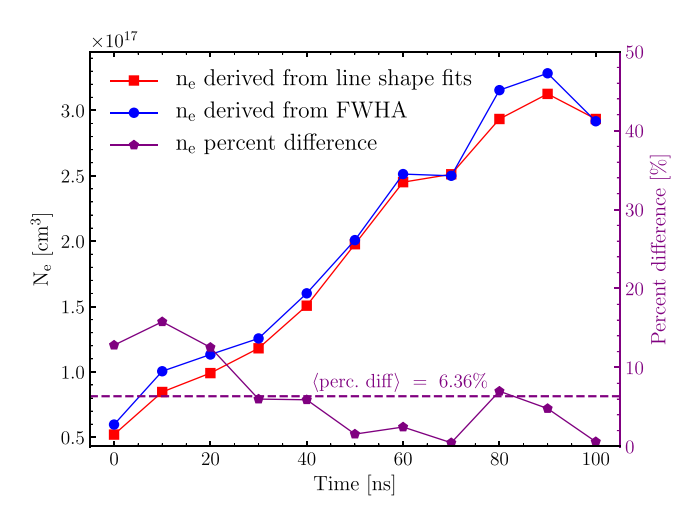


Figure 15. Comparison of $n_{\rm e}$ values inferred from detailed line profile fits to emission-corrected absorption spectra (blue) with the FWHA $n_{\rm e}$ values inferred from uncorrected absorption spectra. The results agree very well. We also show the calculated percent difference between the two methods (purple).

ORCID iDs

M. H. Montgomery https://orcid.org/0000-0002-6748-1748

References

Agertz, O., & Kravtsov, A. V. 2015, ApJ, 804, 18
Bailey, J. E., Chandler, G. A., Mancini, R. C., et al. 2006, PhPl, 13, 056301
Bengtson, R. D., Miller, M. H., Davis, W. D., & Greig, J. R. 1969, ApJ, 157, 957

Berg, H. F., Ali, A. W., Lincke, R., & Griem, H. R. 1962, PhRv, 125, 199 Bergeron, P. 1993, ASIC, 403, 267

Bergeron, P., Dufour, P., Fontaine, G., et al. 2019, ApJ, 876, 67

Bergeron, P., Saffer, R. A., & Liebert, J. 1992, ApJ, 394, 228

Cummings, J. D., Kalirai, J. S., Choi, J., et al. 2019, ApJL, 871, L18

Cummings, J. D., Kalirai, J. S., Tremblay, P.-E., & Ramirez-Ruiz, E. 2015, ApJ, 807, 90

Cummings, J. D., Kalirai, J. S., Tremblay, P.-E., & Ramirez-Ruiz, E. 2016, ApJ, 818, 84

Cummings, J. D., Kalirai, J. S., Tremblay, P.-E., & Ramirez-Ruiz, E. 2018, PhRvA, 98, 012505

Falcon, R. E. 2014, PhD thesis, Univ. Texas

```
Falcon, R. E., Bliss, D. E., & Carlson, A. L. 2015a, Tech. Rep. SAND2015-
   3955, (Albuquerque, NM: Sandia National Laboratories)
Falcon, R. E., Rochau, G. A., Bailey, J. E., et al. 2013, HEDP, 9, 82
Falcon, R. E., Rochau, G. A., Bailey, J. E., et al. 2015b, ApJ, 806, 214
Falcon, R. E., Winget, D. E., Montgomery, M. H., & Williams, K. A. 2010,
   ApJ, 712, 585
Fontaine, G., Brassard, P., & Bergeron, P. 2001, PASP, 113, 409
Fuchs, J. T. 2017, PhD thesis, Univ. North Carolina
Gaia Collaboration, Prusti, T., de Bruijne, J. H. J., et al. 2016, A&A, 595, A1
Genest-Beaulieu, C., & Bergeron, P. 2019, ApJ, 871, 169
Gentile Fusillo, N. P., Tremblay, P.-E., Gänsicke, B. T., et al. 2019, MNRAS,
   482, 4570
Gigosos, M. A., & Cardeñoso, V. 1996, JPhB, 29, 4795
Gigosos, M. A., González, M. Á., & Cardeñoso, V. 2003, AcSpe, 58, 1489
Gomez, T. A. 2017, PhD thesis, Univ. Texas, http://hdl.handle.net/2152/61767
Gomez, T. A., Nagayama, T., Kilcrease, D. P., Montgomery, M. H., &
  Winget, D. E. 2016, PhRvA, 94, 022501
Gomez, T. A., Nagayama, T., Kilcrease, D. P., Montgomery, M. H., &
   Winget, D. E. 2018, PhRvA, 98, 012505
Griem, H. R., Kolb, A. C., & Shen, K. Y. 1962, ApJ, 135, 272
Günter, S., Hitzschke, L., & Röpke, G. 1991, PhRvA, 44, 6834
Hill, R. A., Gerardo, J. B., & Kepple, P. C. 1971, PhRvA, 3, 855
Hubeny, I., & Mihalas, D. 2014, Theory of Stellar Atmospheres (Princeton, NJ:
  Princeton Univ. Press)
Kepler, S. O., Pelisoli, I., Koester, D., et al. 2015, MNRAS, 446, 4078
```

```
Jones, M. C., Ampleford, D. J., Cuneo, M. E., et al. 2014, RScI, 85, 083501
Joyce, S. R. G., Barstow, M. A., Holberg, J. B., et al. 2018, MNRAS,
  481, 2361
Koester, D. 2010, MmSAI, 81, 921
Lemke, M. 1997, A&AS, 122, 285
MacFarlane, J. J., Golovkin, I. E., Wang, P., Woodruff, P. R., & Pereyra, N. A.
  2007, HEDP, 3, 181
MacFarlane, J. J., Golovkin, I. E., & Woodruff, P. R. 2006, JQSRT, 99, 381
McDaniel, D. H., Mazarakis, M. G., Bliss, D. E., et al. 2002, in AIP Conf. Proc.
  651, Dense Z-Pinches: 5th Int. Conf. on Dense Z-Pinches, ed. J. Davis,
  C. Deeney, & N. R. Pereira (New York: AIP), 23
Montgomery, M. H., Falcon, R. E., Rochau, G. A., et al. 2015, HEDP, 17, 168
Pasquini, L., Pala, A. F., Ludwig, H.-G., et al. 2019, A&A, 627, L8
Rochau, G. A., Bailey, J. E., Falcon, R. E., et al. 2014, PhPl, 21, 056308
Rose, D. V., Welch, D. R., Madrid, E. A., et al. 2010, PhRvS, 13, 010402
Sanford, T. W. L., Lemke, R. W., Mock, R. C., et al. 2002, PhPl, 9, 3573
Schaeuble, M.-A. 2018, PhD thesis, Univ. Texas, doi:10.26153/tsw/1348
Tremblay, P.-E., & Bergeron, P. 2009, ApJ, 696, 1755
Tremblay, P.-E., Bergeron, P., & Gianninas, A. 2011, ApJ, 730, 128
Tremblay, P.-E., Cukanovaite, E., Gentile Fusillo, N. P., Cunningham, T., &
  Hollands, M. A. 2019, MNRAS, 482, 5222
Vidal, C. R., Cooper, J., & Smith, E. W. 1970, JOSRT, 10, 1011
Vidal, C. R., Cooper, J., & Smith, E. W. 1973, ApJS, 25, 37
Wiese, W. L., Kelleher, D. E., & Paquette, D. R. 1972, PhRvA, 6, 1132
```

Winget, D. E., Hansen, C. J., Liebert, J., et al. 1987, ApJL, 315, L77